IEEE Access
Multidisciplinary ⋮ Rapid Review ⋮ Open Access Journal

Received 23 January 2024, accepted 27 January 2024, date of publication 5 February 2024, date of current version 14 February 2024.

Digital Object Identifier 10.1109/ACCESS.2024.3362674

RESEARCH ARTICLE

Control Strategy for Safety Purposes Based Upon Momentum Regulation

JIAN LIU[1] AND YOJI YAMADA[1,2], (Member, IEEE)
[1]Department of Mechanical Systems Engineering, Nagoya University, Nagoya 464-8603, Japan
[2]Toyota College, National Institute of Technology, Toyota 471-0067, Japan

Corresponding author: Jian Liu (liu.jian.e1@f.mail.nagoya-u.ac.jp)

This work was supported in part by the Ministry of Education, Culture, Sports, Science and Technology, Japan, through the project "Novel Safety Control Strategy at the Time of Collision Under the Worst Condition for a Robot With a Single Fault Detection Capability" under Grant 20H02114; and in part by the Ministry of Economy, Trade and Industry, Japan, through the project "International Standardization of Safety Test Methods for Minor Hand Injuries Based on Actual Use Cases of Human-Collaborating Machines" under Grant SSU53-437-SEN46.

ABSTRACT Ensuring human safety in human–robot collaboration is an active research topic. This paper newly presented that momentum is a quantification parameter to estimate slight injury, and 14.6 N·s was considered as a threshold of the slight injury onset level. Based on this finding, a momentum observer-based control strategy for securing the safety of human body parts in the clamping scenario was originally proposed. The momentum observer and motion reshaping provided a momentum-limit function, helping to avoid the risk associated with the momentum exceeding the threshold. The part of the estimated external momentum that exceeds a predetermined momentum threshold is transformed into a motion trajectory to reshape the command motion and limit the external momentum under the injury onset criterion. Clamping experiments were conducted using a manipulator with seven degrees of freedom and a dummy with high biofidelity. The experimental results show that the external momentum was successfully limited under the momentum threshold that was set as 10 N·s, and a 5 N contact force was reduced to 0 N in the clamping situation. The study exhibits that the proposed control strategy can help avoid the risk of the momentum exceeding an injury onset threshold when the human body part is clamped and can effectively release the human body part in a clamping scenario.

INDEX TERMS Control strategy, momentum injury onset criterion, safety, clamping, human–robot collaboration.

I. INTRODUCTION

Human–robot collaboration systems for manufacturing are in great demand [1] because the combination of humans and robots enhances efficiency as well as production flexibility [2], [3]. However, humans and robots are required to share the same physical environment, significantly increasing the probability of physical human–robot interaction (pHRI) [4]. Therefore, ensuring human safety in human–robot collaboration has become an active research topic. The pHRI can be divided into pre-contact, under-contact, and post-contact stages. The contact can be predicted and avoided in the pre-contact stage, and human safety is secured by detecting and attempting to release the contact in the under-contact stage.

New technologies have emerged to predict and avoid contact by recognizing and modeling the robot's work environment with human operators. Zhdanova et al. [5] proposed an algorithm to recognize actions of human operators using machine vision systems. Unhelkar et al. [6] proposed a semi-supervised algorithm to learn models of human behavior. El-Shamouty et al. [7] presented a framework using Deep Reinforcement Learning to comprehend the environment to make the robot complete a collision-free motion. In [8], the cyber physical system was used to evaluate the safe distance and trigger collision preventive

The associate editor coordinating the review of this manuscript and approving it for publication was Okyay Kaynak.

actions. However, these studies have not been extensively applied to industrial manipulators, and their reliability needs to be improved. In a relatively traditional manner, radio wave sensors [9], laser scanner sensors [10], and inertial measurement units [11] have been used to stop or slow down the manipulator when the human body part that enters the working range of the robot is detected. The methods for predicting and avoiding contact in the pre-contact stage keep the distance between human workers and robots and reduce the motions of robot, which makes the collaboration difficult.

Safe contact in the under-contact stage should be permitted to make human operators and robots closer to make collaboration much easier. The conventional method involves measuring and regulating the contact force to restrict the movement of the manipulator. Active stiffness control [12], [13] was proposed to address a peg-in-hole task in the assembly, and it can be used to reduce the contact force due to a spring property assigned to the end effector. Impedance control [14] is regarded as an extension of the active stiffness control as the virtual impedance assigned to the manipulator is extended as a mass-spring-damper model from a spring model [15]. The virtual impedance can be adjusted to regulate the contact force [16]. However, optimizing the impedance parameters requires the mechanical properties of the human body part. Additionally, the contact force detection loses efficacy if the contact occurs with the links of the manipulator but not with the force sensor on the end effector [17], [18].

Conventional studies on securing human safety were achieved by adding reaction movement to the manipulator after detecting contact. A pioneering work on safety-oriented control methods was proposed by Yamada et al. [19], [20]. The manipulator was designed to stop if the contact force estimated by the observer exceeds the pain tolerance determined through contact experiments with human subjects. Haddadin et al. [21], [22] also mentioned a similar strategy for a safe stop in cases where a torque observer detected the collision. Aivaliotis et al. [23] proposed a method for observing the current of each motor to limit the contact force. Moreover, a stop function is required by a technical specification ISO/TS 15066 [24] to limit the contact force to a safe zone. However, the force-limit method cannot regulate the contact force in the post-contact period and remains the contact force in a clamping situation such that the compressed human body part cannot escape from the clamping situation. Reaction strategies related to gravity compensator, inertia reduction, and admittance control were compared in [21] and [22]. However, the contact force may exceed a criterion if the remaining kinematic energy of the manipulator is large. In [25], the reaction motion for the manipulator was designed as a backward motion against the direction of the observed external toque, but a compositive control method was not presented.

As safer considerations, a more intrinsic mechanism to secure human safety is necessary than equipping a robot with additional sensors, which needs observers to monitor the contact force to replace or cooperate with force sensors. Securing safety only by stopping the robot is one-sided because the human side, unlike the robot side, cannot stop immediately. Based on the above analysis, this study proposes a momentum control method to compensate for the shortage of existing safety control methods by realizing the safety securement on the level of momentum.

This study reveals that the physical quantity of momentum is appropriate as a quantification criterion to estimate a slight injury onset level. Although Haddadin et al. [26] conducted collision experiments and showed that the mass and maximum velocity of the impactor correlated positively with the injury level, the concept of momentum has not taken shape. On the other hand, the momentum controller proposed by Ohnishi et al. [27], [28] was to examine the effectiveness and stability when the manipulator passes through singularity points. However, it lacks functions such as monitoring and reaction for the collision, which is unrelated to the safety-oriented control. This study first shows the usage of the momentum controller for safety, and a modified version is also proposed. The key point for securing safety is to limit the external momentum that denotes the integral of contact force within the momentum injury onset criterion. For this purpose, this study also presents a momentum observer to monitor the external momentum. To the best of the authors' knowledge, there is currently no proposal of observers for estimating momenta. In contrast, observers based on generalized momentum were proposed to estimate the external torque and detect collisions. The earliest study was presented by Luca et al. [29], in which the actuator failure was detected by a first-order state extended observer based on generated momenta to avoid using the acceleration that may not be measurable. This technology was employed for detecting collision by estimating the external torque in [30], [31] and was extended into a second-order state extended observer in [25], [32]. The extended state observers based on momenta were summarized in [33]. Joint frictions were identified in [34], [35], and the slide mode method was developed in [36], [37] to enhance performance estimation. This type of observer should be referred to as a ''momentum-based observer'' rather than a ''momentum observer'' because the observer does not estimate momentum, rather the residual torque (that is, the external torque generated by the contact force). The observer proposed in this study shows essential differences in structure and purpose.

In summary, the originality of this study is that it proposes momentum control necessary to ensure safety. It is newly shown that the physical quantity of momentum is appropriate as a quantification criterion when considering the occurrence or non-occurrence of a slight injury as a limit of intrinsic safety. Furthermore, the momentum observer is incorporated as part of the control strategy to provide a momentum-limit function that forces the manipulator to retreat from a contact regardless of whether this contact is passive or positive for the manipulator. This control strategy is expected to be integrated

into the industry manipulators to accelerate the human-robot collaboration.

II. MOMENTUM-BASED CONTROL STRATEGY

A. MOMENTUM CRITERION FOR INJURY ONSET LEVEL

The safety of human soft tissue has been discussed based on the contact force, pressure, supplied energy, and criteria related to the vehicle industry. However, momentum has been omitted as an important physical variable in the dynamic system. This section shows the relationship between the momentum and the occurrence of "slight injury" in the impact on the porcine soft tissue. The analysis result was based on the experimental data in the study [38] that include the contact force and velocity of the impactor in time series as well as the label showing the occurrence or nonoccurrence of slight injury in each trial. The experimental method and the estimation of slight injury are detailed in [38].

The computation of momentum was conducted by taking an integral of the contact force along the time over the entire contact process. The result is depicted in Fig. 1. All points with momentum less than 5 N·s were "no slight injury", whereas all points with momentum greater than 25 N·s were "slight injury". When the momentum was between 5 and 25 N·s, both "no slight injury" and "slight injury" were present. A logistical regression model shown in (1) was used to determine the probability of the occurrence of slight injury.

$$p = \frac{1}{1 + e^{-(L-\beta_1)/\beta_2}}, \tag{1}$$

where p denotes the probability of the sight injury occurrence, L the momentum, and β_1 and β_2 the parameters to be optimized.

In curve fitting, the weights for the points with momentum less than 5 N·s and greater than 25 N·s were set to a large value of 100 because the probabilities of slight injury nonoccurrence and slight injury occurrence were considered large, respectively. In contrast, the weights for the points with momentum between 5 and 25 N·s were set to a small value of 1. This setting resulted in a logistical regression curve with $\beta_1 = 67.7$ and $\beta_2 = 3.7$, as shown in Fig. 1. As observed, 14.6 N·s can be considered as an injury onset threshold defining a slight injury onset with 10% in this case by which the risk of causing slight injury is acceptable, that is, safe. We conclude that momentum can be a criterion for estimating whether a slight injury occurs.

B. DYNAMICS OF MANIPULATOR

Without loss of generality, a positive integer n is used to represent the number of degree of freedom (DOF) of a manipulator. The dynamic model of an n-DOF manipulator can be expressed in the following canonical form:

$$\boldsymbol{\tau} = \boldsymbol{M}(\boldsymbol{\theta})\ddot{\boldsymbol{\theta}} + \boldsymbol{C}\left(\boldsymbol{\theta}, \dot{\boldsymbol{\theta}}\right)\dot{\boldsymbol{\theta}} + \boldsymbol{g}(\boldsymbol{\theta}), \tag{2}$$

where $\boldsymbol{\theta} \in \mathcal{R}^n$ denotes the vector of the angular position, $\boldsymbol{M}(\boldsymbol{\theta}) \in \mathcal{R}^{n\times n}$ the inertia matrix, $\boldsymbol{C}(\boldsymbol{\theta}, \dot{\boldsymbol{\theta}}) \in \mathcal{R}^{n\times n}$ the Coriolis and centripetal matrix, $\boldsymbol{g}(\boldsymbol{\theta}) \in \mathcal{R}^n$ the gravity vector, and $\boldsymbol{\tau} \in \mathcal{R}^n$ the net torque vector. According to the Lagrange formulation [39], (2) can be rewritten as follows:

$$\boldsymbol{\tau} = \frac{\mathrm{d}}{\mathrm{d}t}\left(\boldsymbol{M}\dot{\boldsymbol{\theta}}\right) - \frac{\partial}{\partial \boldsymbol{\theta}^T}\left[\frac{1}{2}\dot{\boldsymbol{\theta}}^T\boldsymbol{M}(\boldsymbol{\theta})\dot{\boldsymbol{\theta}}\right] + \boldsymbol{g}(\boldsymbol{\theta}). \tag{3}$$

According to [29], the second term on the right-hand side of (3) is related to $\boldsymbol{C}(\boldsymbol{\theta}, \dot{\boldsymbol{\theta}})$ as

$$\frac{\partial}{\partial \boldsymbol{\theta}^T}\left[\frac{1}{2}\dot{\boldsymbol{\theta}}^T\boldsymbol{M}(\boldsymbol{\theta})\dot{\boldsymbol{\theta}}\right] = \boldsymbol{C}^T\left(\boldsymbol{\theta}, \dot{\boldsymbol{\theta}}\right)\dot{\boldsymbol{\theta}}, \tag{4}$$

and the joint-space momentum $\boldsymbol{M}\dot{\boldsymbol{\theta}}$ in (3) is related to the operational-space momentum ${}^{\Sigma}\boldsymbol{M}\dot{\boldsymbol{x}}$ as follows:

$$\boldsymbol{M}\dot{\boldsymbol{\theta}} = \boldsymbol{J}^{T\,\Sigma}\boldsymbol{M}\dot{\boldsymbol{x}}, \tag{5}$$

where ${}^{\Sigma}\boldsymbol{M} \in \mathcal{R}^{6\times 6}$ and $\dot{\boldsymbol{x}} \in \mathcal{R}^6$ denote the mass matrix and velocity of the end effector, respectively, and $\boldsymbol{J} \in \mathcal{R}^{6\times n}$ is the Jacobian matrix. Therefore, (3) can be rewritten as

$$\boldsymbol{\tau} = \frac{\mathrm{d}}{\mathrm{d}t}\left(\boldsymbol{J}^{T\,\Sigma}\boldsymbol{M}\dot{\boldsymbol{x}}\right) - \boldsymbol{C}^T\left(\boldsymbol{\theta}, \dot{\boldsymbol{\theta}}\right)\dot{\boldsymbol{\theta}} + \boldsymbol{g}(\boldsymbol{\theta}). \tag{6}$$

The net torque vector $\boldsymbol{\tau} \in \mathcal{R}^n$ in (3) and (6) is a superposition as

$$\boldsymbol{\tau} = \boldsymbol{\tau}_{\mathrm{ref}} - \boldsymbol{\tau}_{\mathrm{ext}} - \boldsymbol{\tau}_{\mathrm{dis}}, \tag{7}$$

where $\boldsymbol{\tau}_{\mathrm{ref}} \in \mathcal{R}^n$ is the reference torque generated by the controller, $\boldsymbol{\tau}_{\mathrm{dis}} \in \mathcal{R}^n$ the disturbance including noise, and $\boldsymbol{\tau}_{\mathrm{ext}} \in \mathcal{R}^n$ the torque contributed by the contact force $\boldsymbol{F}_{\mathrm{ext}} \in \mathcal{R}^6$. The relationship between $\boldsymbol{\tau}_{\mathrm{ext}}$ and $\boldsymbol{F}_{\mathrm{ext}}$ is

$$\boldsymbol{\tau}_{\mathrm{ext}} = \boldsymbol{J}^T\boldsymbol{F}_{\mathrm{ext}}. \tag{8}$$

Subsequently, the external momentum $\boldsymbol{L}_{\mathrm{ext}} \in \mathcal{R}^6$ is defined as the integral of the contact force as follows:

$$\boldsymbol{L}_{\mathrm{ext}} = \int \boldsymbol{F}_{\mathrm{ext}}\mathrm{d}t. \tag{9}$$

The matrices $\hat{\boldsymbol{M}}$ and $\hat{\boldsymbol{C}}$ along with the vector $\hat{\boldsymbol{g}}$ denote the estimation of $\boldsymbol{M}$, $\boldsymbol{C}$, and $\boldsymbol{g}$ and are computed using a modified Newton–Euler recursion method, referring to [40].

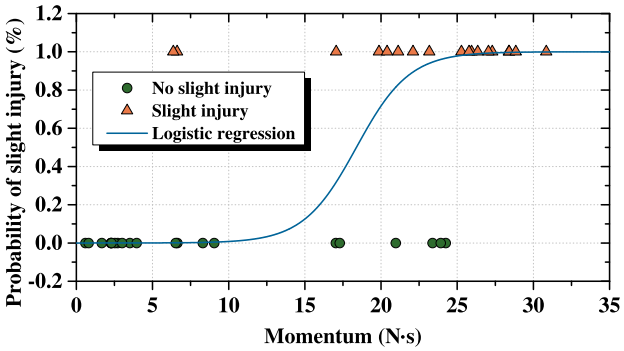

FIGURE 1. Relationship between momentum and probability of slight injury occurrence.

C. CONTROL STRATEGY

The proposed control strategy in this study adjusts the external momentum below the momentum injury criteria. Therefore, developing an external momentum observer is convenient if the momentum signal can be included in the main control loop. The momentum controller with compensator is as follows:

$$\boldsymbol{\tau}_{\text{ref}} = \frac{\mathrm{d}}{\mathrm{d}t}\left(\boldsymbol{J}^T \boldsymbol{L}_{\text{ref}}\right) - \hat{\boldsymbol{C}}^T(\boldsymbol{\theta}, \dot{\boldsymbol{\theta}})\,\dot{\boldsymbol{\theta}} + \hat{\boldsymbol{g}}(\boldsymbol{\theta}), \tag{10}$$

$$\boldsymbol{L}_{\text{ref}} = {}^{\Sigma}\hat{\boldsymbol{M}} \int \left({}^{\Sigma}\boldsymbol{K}_{\text{p}}\,{}^{\Sigma}\boldsymbol{e} + {}^{\Sigma}\boldsymbol{K}_{\text{d}}\,{}^{\Sigma}\dot{\boldsymbol{e}} + \ddot{\boldsymbol{x}}_{\text{cmd}}\right)\mathrm{d}t + \hat{\boldsymbol{L}}_{\text{ext}}, \tag{11}$$

$${}^{\Sigma}\boldsymbol{e} = \boldsymbol{x}_{\text{cmd}} - \boldsymbol{x}, \tag{12}$$

where $\boldsymbol{x} \in \mathcal{R}^6$ denotes the position and orientation of the end effector, $\boldsymbol{x}_{\text{cmd}} \in \mathcal{R}^6$ the command trajectory in the operational space, ${}^{\Sigma}\boldsymbol{e} \in \mathcal{R}^6$ the error term, and ${}^{\Sigma}\hat{\boldsymbol{M}} \in \mathcal{R}^{6\times 6}$ the estimation of ${}^{\Sigma}\boldsymbol{M}$. Matrices ${}^{\Sigma}\boldsymbol{K}_{\text{p}}$, ${}^{\Sigma}\boldsymbol{K}_{\text{d}} \in \mathcal{R}^{6\times 6}$ are diagonal and denote the proportional and derivative gains, respectively.

The external momentum is defined as a variable representing the integral of the contact force as shown in (9), and a second-order observer is proposed to estimate it. The structure of the observer is as follows:

$$\tilde{\boldsymbol{L}} = \boldsymbol{L}_{\text{ref}} - {}^{\Sigma}\hat{\boldsymbol{M}}\dot{\boldsymbol{x}}, \tag{13}$$

$$\hat{\boldsymbol{F}}_{\text{ext}} = {}^{\Sigma}\boldsymbol{K}_1 \int \left(\tilde{\boldsymbol{L}} - \hat{\boldsymbol{L}}_{\text{ext}}\right)\mathrm{d}t + {}^{\Sigma}\boldsymbol{K}_2\left(\tilde{\boldsymbol{L}} - \hat{\boldsymbol{L}}_{\text{ext}}\right), \tag{14}$$

$$\hat{\boldsymbol{L}}_{\text{ext}} = \int \hat{\boldsymbol{F}}_{\text{ext}}\mathrm{d}t, \tag{15}$$

where ${}^{\Sigma}\boldsymbol{K}_1$, ${}^{\Sigma}\boldsymbol{K}_2 \in \mathcal{R}^{6\times 6}$ denote the gain matrices, and $\hat{\boldsymbol{F}}_{\text{ext}}$ represents the estimated contact force.

The command trajectory is reshaped to adjust and limit the external momentum below the momentum injury onset threshold. The momentum in the estimated external momentum $\boldsymbol{L}_{\text{ext}}$ that exceeds the momentum injury onset threshold $\boldsymbol{L}_{\text{index}}$ is defined as $\boldsymbol{L}_{\text{adj}}$, which is expressed as follows:

$$\boldsymbol{L}_{\text{adj}} = \begin{cases} \boldsymbol{0}, & \hat{\boldsymbol{L}}_{\text{ext}} \le \boldsymbol{L}_{\text{index}} \\ \hat{\boldsymbol{L}}_{\text{ext}} - \boldsymbol{L}_{\text{index}}, & \hat{\boldsymbol{L}}_{\text{ext}} > \boldsymbol{L}_{\text{index}} \end{cases}. \tag{16}$$

The reshaped command trajectory $\boldsymbol{x}_{\text{rsp}}$ is the updated command for the controller:

$$\boldsymbol{x}_{\text{rsp}} = \boldsymbol{x}_{\text{cmd}} - \int {}^{\Sigma}\hat{\boldsymbol{M}}_{\text{inv}}\boldsymbol{L}_{\text{adj}}\mathrm{d}t, \tag{17}$$

where ${}^{\Sigma}\hat{\boldsymbol{M}}_{\text{inv}}$ is the inverse of the estimated mass matrix ${}^{\Sigma}\hat{\boldsymbol{M}}$. Owing to the motion reshaping, the command trajectory $\boldsymbol{x}_{\text{cmd}}$ in (11) and (12) is replaced by the reshaped trajectory $\boldsymbol{x}_{\text{rsp}}$. Thus, (11) and (12) are then expressed as follows:

$$\boldsymbol{L}_{\text{ref}} = {}^{\Sigma}\hat{\boldsymbol{M}} \int \left({}^{\Sigma}\boldsymbol{K}_{\text{p}}\,{}^{\Sigma}\boldsymbol{e} + {}^{\Sigma}\boldsymbol{K}_{\text{d}}\,{}^{\Sigma}\dot{\boldsymbol{e}} + \ddot{\boldsymbol{x}}_{\text{rsp}}\right)\mathrm{d}t + \hat{\boldsymbol{L}}_{\text{ext}}, \tag{18}$$

$${}^{\Sigma}\boldsymbol{e} = \boldsymbol{x}_{\text{rsp}} - \boldsymbol{x}. \tag{19}$$

Normally, the estimated mass matrix ${}^{\Sigma}\hat{\boldsymbol{M}}$ is calculated using the inverse of the Jacobian matrix as ${}^{\Sigma}\hat{\boldsymbol{M}} = \boldsymbol{J}^{-T}\hat{\boldsymbol{M}}\boldsymbol{J}^{-1}$. However, knowing that the inverse of the estimated mass matrix $\hat{\boldsymbol{M}}_{\text{inv}}$ is needed in (17), ${}^{\Sigma}\hat{\boldsymbol{M}}$ can be obtained by taking the inverse of ${}^{\Sigma}\hat{\boldsymbol{M}}_{\text{inv}}$. The matrix $\hat{\boldsymbol{M}}_{\text{inv}}$ is obtained as follows:

$${}^{\Sigma}\hat{\boldsymbol{M}}_{\text{inv}} = \boldsymbol{J}\hat{\boldsymbol{M}}^{-1}\boldsymbol{J}^T, \tag{20}$$

and the matrix ${}^{\Sigma}\hat{\boldsymbol{M}}$ is then obtained by

$${}^{\Sigma}\hat{\boldsymbol{M}} = \begin{cases} \left[{}^{\Sigma}\hat{\boldsymbol{M}}_{\text{inv}} + \left(\mu - \det\left({}^{\Sigma}\hat{\boldsymbol{M}}_{\text{inv}}\right)\boldsymbol{I}\right)\right]^{-1}, & \det\left({}^{\Sigma}\hat{\boldsymbol{M}}_{\text{inv}}\right) < \mu \\ \left({}^{\Sigma}\hat{\boldsymbol{M}}_{\text{inv}}\right)^{-1}, & \det\left({}^{\Sigma}\hat{\boldsymbol{M}}_{\text{inv}}\right) \ge \mu, \end{cases} \tag{21}$$

where μ is a threshold value for making the inverse computation realizable if the determinant of ${}^{\Sigma}\hat{\boldsymbol{M}}_{\text{inv}}$ is nearly zero when the manipulator moves close to the singularity points, and $\boldsymbol{I} \in \mathcal{R}^{6\times 6}$ is an identity matrix.

Equations (10) and (13)–(19) are illustrated in the block diagram of Fig. 2. The entire control strategy is summarized in three parts: controller loop, momentum observer, and motion reshaping. The controller converts the signal generated by a proportional–derivative (PD) controller into the operational-space momentum by pre-multiplying ${}^{\Sigma}\hat{\boldsymbol{M}}$, into the joint-space momentum by pre-multiplying $\boldsymbol{J}^T$, and then into the torque signal by taking a derivative. The momentum observer estimates the operational-space external momentum, which is fed into the controller loop to compensate for the external momentum to enhance the stiffness of the PD controller. The motion reshaping limits the momentum reference $\boldsymbol{L}_{\text{ref}}$ within a momentum injury onset threshold. Specifically, the part in the estimated external momentum that exceeds the momentum injury onset threshold is transformed into a motion signal to modify the command motion trajectory. This is based on the property of the momentum variable: momentum is the product of mass and velocity, as well as the integral of force.

D. PERFORMANCE ESTIMATION

The error dynamics is obtained by combining (6)–(10), (18), and (19), as follows:

$${}^{\Sigma}\boldsymbol{e} = \frac{s}{s^2 + s\,{}^{\Sigma}\boldsymbol{K}_{\text{d}} + {}^{\Sigma}\boldsymbol{K}_{\text{p}}}\,{}^{\Sigma}\hat{\boldsymbol{M}}^{-1}\left(\boldsymbol{L}_{\text{ext}} - \hat{\boldsymbol{L}}_{\text{ext}} + \boldsymbol{\eta}\right), \tag{22}$$

where $\boldsymbol{\eta}$ is

$$\begin{aligned} \boldsymbol{\eta} = {} & \left({}^{\Sigma}\boldsymbol{M} - {}^{\Sigma}\hat{\boldsymbol{M}}\right)\dot{\boldsymbol{x}} \\ & + \boldsymbol{J}^{-T}\int\left[-\left(\boldsymbol{C}^T - \hat{\boldsymbol{C}}^T\right)\dot{\boldsymbol{\theta}} + \left(\boldsymbol{g} - \hat{\boldsymbol{g}}\right)\right]\mathrm{d}t \\ & + \int\left(\dot{\boldsymbol{J}}^{-T}\int \boldsymbol{J}^T\boldsymbol{F}_{\text{ext}}\mathrm{d}t\right)\mathrm{d}t + \boldsymbol{J}^{-T}\int\boldsymbol{\tau}_{\text{dis}}\mathrm{d}t. \end{aligned} \tag{23}$$

On the right-hand side of (23), the first two terms are the modeling errors, and the last term is the noise. The third term can be neglected because the derivative of the Jacobian matrix $\dot{\boldsymbol{J}}$ approximates a null matrix if the manipulator moves slowly or stops moving.

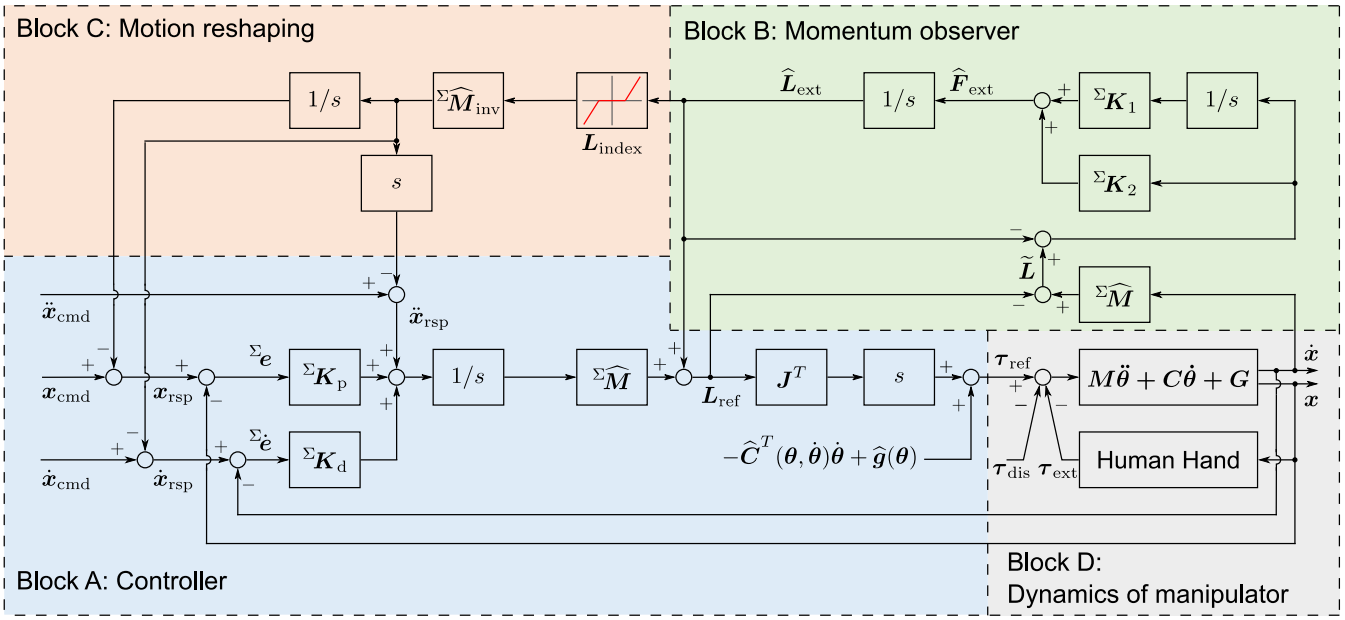

FIGURE 2. Block diagram of safety-oriented control strategy. Block A (light blue) is the controller loop, block B (light green) the momentum observer, block C (light red) the motion reshaping, and block D (light gray) the dynamics of the manipulator and environment.

The momentum variable is included in the controller loop as a reference signal for the motors. By compensating for gravity along with a part of the Coriolis and centrifugal forces, the external momentum can be simply estimated by subtracting the momentum contributed by the manipulator motion ${}^{\Sigma}\boldsymbol{M}\dot{\boldsymbol{x}}$ from the reference momentum $\boldsymbol{L}_{\mathrm{ref}}$, as shown in (13). Combining (7)–(10) and (13)–(15), the relationship between $\hat{\boldsymbol{L}}_{\mathrm{ext}}$ and $\boldsymbol{L}_{\mathrm{ext}}$ is expressed as follows:

$$\hat{\boldsymbol{L}}_{\mathrm{ext}} = \frac{s{}^{\Sigma}\boldsymbol{K}_2 + {}^{\Sigma}\boldsymbol{K}_1}{s^2 + s{}^{\Sigma}\boldsymbol{K}_2 + {}^{\Sigma}\boldsymbol{K}_1}\left(\boldsymbol{L}_{\mathrm{ext}} + \boldsymbol{\eta}\right). \tag{24}$$

The transfer function containing matrices ${}^{\Sigma}\boldsymbol{K}_1$ and ${}^{\Sigma}\boldsymbol{K}_2$ can be regarded as a second-order low-pass filter. Therefore, the estimated external momentum is a filtered signal of the external momentum by this second-order low-pass filter. Due to the presence of $\boldsymbol{\eta}$ in (24), it is concluded that the modeling error is the main factor affecting the estimation accuracy.

In our previous study [41], the momentum observer had the following form:

$$\hat{\boldsymbol{L}}_{\mathrm{ext}} = \frac{{}^{\Sigma}\boldsymbol{K}_1}{s^2 + s{}^{\Sigma}\boldsymbol{K}_2 + {}^{\Sigma}\boldsymbol{K}_1}\left(\boldsymbol{L}_{\mathrm{ext}} + \boldsymbol{\eta}\right). \tag{25}$$

Comparing (24) and (25), the performance of the momentum observer is improved by adding the term $s{}^{\Sigma}\boldsymbol{K}_2$ to the numerator of the transfer function.

The effect of motion reshaping is discussed by analyzing the reference signal. Combining (6)–(10), (17), and (19), the reference momentum $\boldsymbol{L}_{\mathrm{ref}}$ becomes

$$\boldsymbol{L}_{\mathrm{ref}} = {}^{\Sigma}\hat{\boldsymbol{M}}\dot{\boldsymbol{x}}_{\mathrm{cmd}} + \boldsymbol{L}_{\mathrm{ext}} - \boldsymbol{L}_{\mathrm{adj}} + \boldsymbol{\eta} - {}^{\Sigma}\hat{\boldsymbol{M}}\dot{\boldsymbol{e}}. \tag{26}$$

When the motion-reshaping function works and the estimated external momentum exceeds the injury onset threshold, $\boldsymbol{L}_{\mathrm{adj}}$ is computed as the second condition of (16). Therefore, (26) can be written as

$$\begin{aligned}\boldsymbol{L}_{\mathrm{ref}} &= {}^{\Sigma}\hat{\boldsymbol{M}}\dot{\boldsymbol{x}}_{\mathrm{cmd}} + \boldsymbol{L}_{\mathrm{index}} + \boldsymbol{L}_{\mathrm{ext}} - \hat{\boldsymbol{L}}_{\mathrm{ext}} + \boldsymbol{\eta} - {}^{\Sigma}\hat{\boldsymbol{M}}\dot{\boldsymbol{e}} \\ &\approx {}^{\Sigma}\hat{\boldsymbol{M}}\dot{\boldsymbol{x}}_{\mathrm{cmd}} + \boldsymbol{L}_{\mathrm{index}},\end{aligned} \tag{27}$$

where the term $\boldsymbol{L}_{\mathrm{ext}} - \hat{\boldsymbol{L}}_{\mathrm{ext}}$ is approximately zero, considering that the momentum observer performs well, and the terms ${}^{\Sigma}\hat{\boldsymbol{M}}\dot{\boldsymbol{e}}$ and $\boldsymbol{\eta}$ are neglected as they are considerably small compared to the other terms.

III. EXPERIMENT DESIGN

Normally, pHRIs are divided into free-bumping and clamping types; the latter is the worst case [42]. In a clamping scenario, the human body part is sandwiched between an approaching machine and an obstacle such that it cannot escape from such a hazardous state [42]. A fixing-bolt task can be considered to be a simple but frequent clamping case of the human–robot cooperation system. As shown in Fig. 3, a manipulator moves a nut runner to fix the hexagonal bolts, whereas a human operator needs to check the state of the bolts and hold the electric wires to prevent damage. A possible and frequent hazard is that the human hand is clamped between the nut runner and the assembly parts. Our proposed control strategy ensures human safety in such a clamping scenario. To this end, an experiment was designed to replicate the clamping cases of the pHRI and to demonstrate the effectiveness of the proposed control strategy.

A. REDESIGNING OF CRANE-X7 MANIPULATOR

In the experiment, the CRANE-X7 manipulator (RT Corp., Japan) was employed to test the effectiveness of the proposed

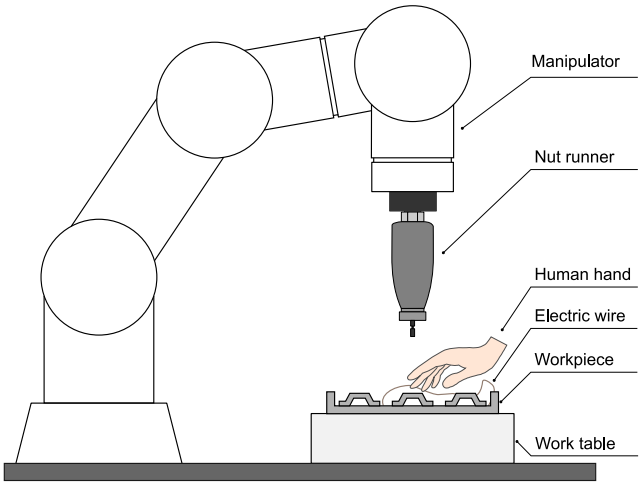

FIGURE 3. Fixing-bolt task work in the human–robot cooperation system.

TABLE 1. Geometric parameters of the redesigned CRANE-X7 manipulator.

Joint number	Geometric parameters			
i	a_i (m)	α_i (rad)	θ_i (rad)	d_i (m)
1	0	0	θ_1	0.105
2	0	$\pi/2$	θ_2	0.000
3	0	$-\pi/2$	θ_3	0.250
4	0	$\pi/2$	θ_4	0.000
5	0	$-\pi/2$	θ_5	0.250
6	0	$\pi/2$	θ_6	0.000
7	0	$-\pi/2$	θ_7	0.095

control strategy. CRANE-X7 has eight rotational joints, and its end effector is a two-finger gripper actuated by the eighth joint. However, the end effector was changed from the gripper to an impactor to fit the clamping experiment. The impactor was designed as a hexagonal prism to mimic the end tip of a nut runner, and its intersecting surface was a hexagon with a circumradius of 3 mm, as shown in Fig. 4(a). The impactor was fixed to the rotor of the seventh motor using two flanges. Therefore, the redesigned CRANE-X7 manipulator had seven DOFs.

The Denavit–Hartenberg (DH) convention method was used to describe the geometric structure of the modified CRANE-X7 manipulator. The geometric description is shown in Fig. 4(b). The base frame is denoted by Σ_0, whereas the frame for the ith joint is denoted by Σ_i. Frames Σ_1 and Σ_2 have the same origin, and likewise for frames Σ_3 and Σ_4, and frames Σ_5 and Σ_6. The geometric parameters are listed in Table 1. a_i denotes the distance between origins of the frames Σ_{i-1} and Σ_i along axis x_{i-1}, and α_i denotes the angle between the axes z_{i-1} and z_i about axis x_{i-1}. d_i denotes the distance between origins of the frames Σ_{i-1} and Σ_i along axis z_i, and θ_i denotes the angular position of the ith joint. Establishing a kinematic model by the DH method through homogeneous transformation matrices is detailed in [43]. The parameter settings and motion commands were the same for all the three patterns.

B. EXPERIMENT SETUP

The experimental setup is shown in Fig. 5. A urethane dummy was used as a substitute for human soft tissue owing to ethical considerations: unexpected instability may appear in the development stage of the control strategy, and the instability can cause hazardous contact with the human soft tissue. However, the feasibility of the control strategy can be guaranteed by using our developed dummy because it has an impedance highly similar to that of the human soft tissue, referring to our previous studies [44], [45]. A six-axis force sensor (WEF-6A200-4-RCD, WACOH-TECH Inc., Japan) measured the contact force and wrench along the x-, y-, and z-axis. The manipulator was fastened to a workbench. Consequently, the workbench, plate, six-axis force sensor, another plate, and dummy were fastened to each other in the mentioned sequence.

The contact point was set at (320.43, 0, 70) mm in the base coordinate. It was located at the center of the upper surface of the dummy and on the centerline of the force sensor. The initial posture of the manipulator was set as 0°, −20°, 0°, −90°, 0°, −70°, and 0° for joints one to seven. At the beginning of the motion, the end effector was kept at the initial position and posture for 2.2 s. Later, it was moved downward along the $-z$ direction to contact and compress the dummy. Finally, the test was terminated after the end effector was maintained at a compressive displacement of 10 mm for 5 s. The posture of the end effector and its position on the x- and y-axis remained unchanged. The velocity was set to 250 mm/s, the maximum velocity recommended in the ISO/TS 15066 document [24] for the machine to contact human soft tissue. The blue curve illustrates the motion trajectory command in Fig. 8. Three patterns were designed as follows:

- Pattern I. Only the controller (block A in Fig. 2), but no motion reshaping and compensation from the momentum observer.
- Pattern II. The controller and compensation from the momentum observer (blocks A and B in Fig. 2), but no motion reshaping.
- Pattern III. The controller, compensation from the momentum observer, and motion reshaping (blocks A, B, and C in Fig. 2).

In this setting, the effectiveness of the momentum observer was shown by comparing the results of Patterns I and II, and the effectiveness of the motion reshaping was shown by comparing the results of Patterns II and III.

The settings of the gain matrices ${}^{\Sigma}\boldsymbol{K}_{\mathrm{p}}$, ${}^{\Sigma}\boldsymbol{K}_{\mathrm{d}}$, ${}^{\Sigma}\boldsymbol{K}_1$, ${}^{\Sigma}\boldsymbol{K}_2$, momentum injury onset threshold $\boldsymbol{L}_{\mathrm{index}}$, and threshold μ are listed in Table 2. The kernel of the momentum controller is a PD controller, hence the gain matrices ${}^{\Sigma}\boldsymbol{K}_{\mathrm{p}}$ and ${}^{\Sigma}\boldsymbol{K}_{\mathrm{d}}$ of the momentum controller have an influence on the tracking errors similar to those of the PD controller. A large ${}^{\Sigma}\boldsymbol{K}_{\mathrm{p}}$ results in instability, whereas a small ${}^{\Sigma}\boldsymbol{K}_{\mathrm{p}}$ causes large tracking errors. ${}^{\Sigma}\boldsymbol{K}_{\mathrm{d}}$ can enhance tracking performance; however, a small ${}^{\Sigma}\boldsymbol{K}_{\mathrm{d}}$ is necessary because it enlarges the noise

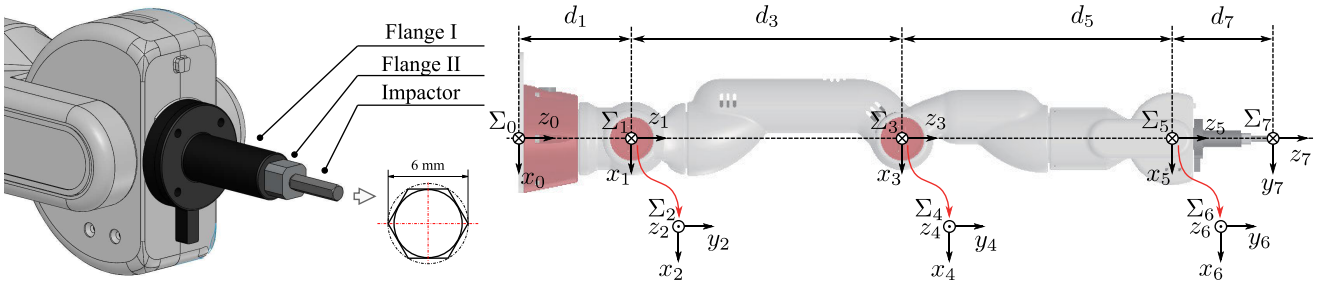

(a) End effector. (b) Geometric description.

FIGURE 4. (a) Hexagonal prism impactor as the end effector of the redesigned CRANE-X7 manipulator. The impactor was attached to the rotor of the seventh motor using two flanges. The bottom right image shows the intersecting surface (or left view) of the impactor as a hexagon with a circumradius of 3 mm. (b) Geometric description of the modified manipulator using the DH method.

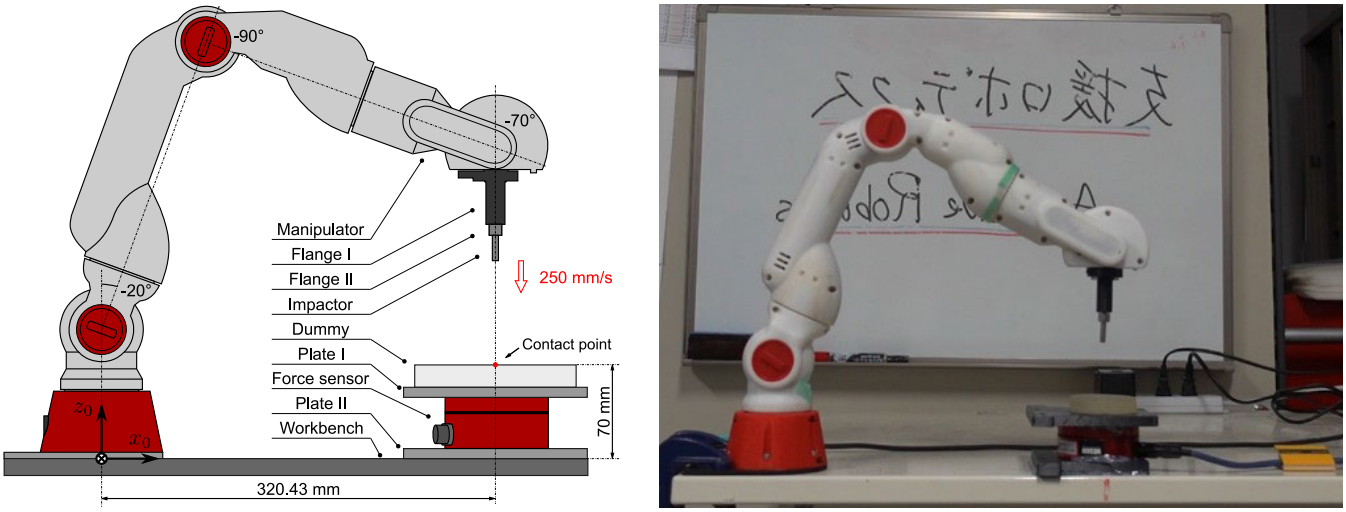

(a) (b)

FIGURE 5. Experiment setup. Joints one to seven are 0°, −20°, 0°, −90°, 0°, −70°, and 0°, which comprise the initial posture in the downward motion. The red point on the upper surface of the dummy represents the contact point.

TABLE 2. Parameter settings.

Parameter	Value
${}^{\Sigma}\boldsymbol{K}_{\mathrm{p}}$	$\mathrm{diag}([2000\ 2000\ 2000\ 2000\ 2000\ 2000]^T)$
${}^{\Sigma}\boldsymbol{K}_{\mathrm{d}}$	$\mathrm{diag}([25\ 25\ 25\ 25\ 25\ 25]^T)$
${}^{\Sigma}\boldsymbol{K}_1$	$\mathrm{diag}([49\ 49\ 49\ 49\ 49\ 49]^T)$
${}^{\Sigma}\boldsymbol{K}_2$	$\mathrm{diag}([14\ 14\ 14\ 14\ 14\ 14]^T)$
$\boldsymbol{L}_{\mathrm{index}}$	$\mathrm{diag}([10\ 10\ 10\ 10\ 10\ 10]^T)$
μ	0.01

in the differential of angular position. In the experiment, ${}^{\Sigma}\boldsymbol{K}_{\mathrm{p}}$ and ${}^{\Sigma}\boldsymbol{K}_{\mathrm{d}}$ were determined by trial and error. The gain matrices ${}^{\Sigma}\boldsymbol{K}_1$ and ${}^{\Sigma}\boldsymbol{K}_2$ determine the cutoff frequency of the momentum observer, and a 2.76 Hz cutoff frequency was set in the experiment. This experiment examined whether the control strategy can provide a performance on limiting the external momentum under a threshold; thus, the momentum injury onset threshold $\boldsymbol{L}_{\mathrm{index}}$ was arbitrarily set to 10 N·s.

IV. EXPERIMENT RESULT

The position and orientation tracking errors are shown in Fig. 6. Errors had similar variations: approximated 0 for 0–2.2 s, increased during 2.2–2.5 s, and attained a stable value from 2.5 s onward. The variation of tracking errors is summarized in TABLE 3. Comparing Figs. 6(a) and 6(c), the steady-state error on the z-axis was −3 mm in Pattern I but was suppressed to 0 mm in Pattern II. The steady-state error on the x-axis decreased from −1 mm to 0.5 mm. A constant steady-state error of approximately −1 mm was obtained on the y-axis in Patterns I and II. Feeding the estimated external momentum decreases the steady-state potion errors on the x- and z-axis but shows low effectiveness on the y-axis. Comparing Figs. 6(b) and 6(d), a maximum instantaneous error of approximately 1.432° (0.025 rad) was obtained on the y-axis, whereas a maximum steady-state error of approximately 0.573° (0.01 rad) was obtained on the x-axis. Feeding the estimated external momentum decreases the steady-state orientation error on the z-axis. However, low effectiveness was obtained on the x- and y-axis.

A comparison between the observed and measured external momenta is presented in Fig. 7. The measured external momentum means the integral of the measured contact force by the force sensor. For brevity, only the external momentum on the z-axis is shown, that is, the third

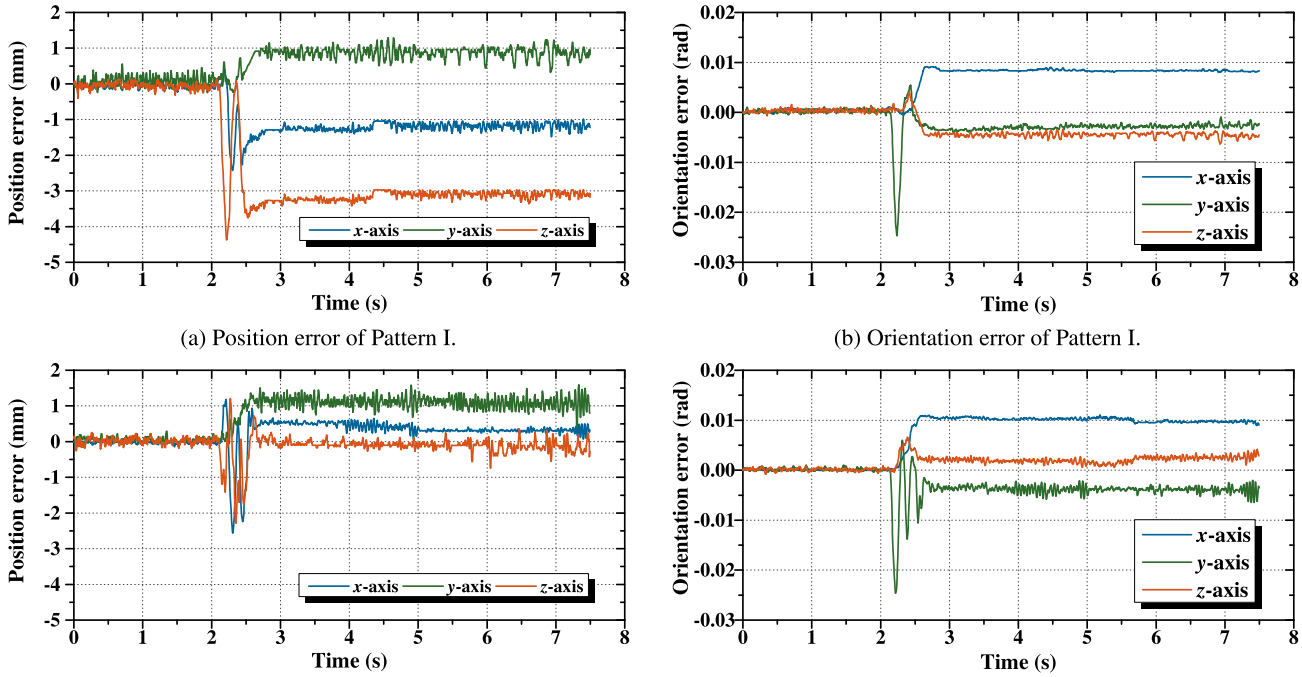

(a) Position error of Pattern I.

(b) Orientation error of Pattern I.

(c) Position error of Pattern II.

(d) Orientation error of Pattern II.

FIGURE 6. Tracking error of Patterns I and II.

component of the vector $\hat{\boldsymbol{L}}_{\text{ext}}$ and the integral of the measured contact force on the z-axis. The observed momentum was close to the measured value for both Patterns II and III. The momentum observer performed well in estimating the external momentum.

The estimation error appeared from 0 to 2.4 s in both Patterns II and III and from 4.5 to 7.5 s in Pattern III. However, as the measured external momentum increased, the estimated external momentum increased in advance compared to the measured one.

The reshaped motion command is illustrated in Fig. 8(a). The motion command was set as 60 mm from 2.5 to 7.5 s; a compressive displacement of 10 mm was maintained for 5 s. The estimated external momentum increased from 2.5 s owing to a positive contact force and exceeded the predetermined momentum injury onset threshold of 10 N·s at approximately 4.4 s, as shown in Fig. 8(b). The motion-reshaping function was triggered at 4.4 s, and the reshaped motion command increased to approximately 74 mm at 4.5 s. The position of 74 mm was higher than the contact point at 70 mm. That is, the impactor moved backward along the z-axis and departed from the dummy. This result coincides with the observations in Figs. 7(b) and 6(b) corresponding to a contact force of 0 N and a constant external momentum, respectively.

V. DISCUSSION

A. CONTROLLER LOOP

The controller loop kept the stability of the manipulator, and the motion trajectory tracking was realized. The momentum controller with compensation $-\hat{\boldsymbol{C}}^T(\boldsymbol{\theta}, \dot{\boldsymbol{\theta}})\dot{\boldsymbol{\theta}} + \hat{\boldsymbol{g}}(\boldsymbol{\theta})$, was stable in a gravity and contact environment, consistent with the finding in [46] that a PD controller with a gravity compensator performs well in a nonexternal force environment.

A steady-state error exists without an integral term in the PD controller in a contact environment or when the manipulator is subjected to an external force. As shown in (18), the momentum controller includes a proportional and derivative term but lacks an integral term to eliminate the steady-state error.

In a contact situation, the external momentum $\boldsymbol{L}_{\text{ext}}$ is the main factor because it is significantly larger than the term $\boldsymbol{\eta}$. The estimated external momentum $\boldsymbol{L}_{\text{ext}}$ is equal to zero when there is no compensation from the estimated external momentum. The terms $\boldsymbol{L}_{\text{ext}}$ and $\boldsymbol{\eta}$ in (22) are neglected to analyze the error in Pattern I. According to the final-value theorem, the tracking error ${}^{\Sigma}\boldsymbol{e}$ converges to a steady-state phase as ${}^{\Sigma}\boldsymbol{K}_{\text{p}}^{-1}{}^{\Sigma}\hat{\boldsymbol{M}}^{-1}\boldsymbol{F}_{\text{ext}}$, indicating that a steady-state error exists due to the contact force.

When the momentum observer performs well, the estimated external momentum approximates the external momentum, $\hat{\boldsymbol{L}}_{\text{ext}} \approx \boldsymbol{L}_{\text{ext}}$. Therefore, the estimated value compensates for the external momentum, and the steady-state error is suppressed by feeding the estimated external momentum $\hat{\boldsymbol{L}}_{\text{ext}}$ into the main loop. The term $\boldsymbol{L}_{\text{ext}} - \hat{\boldsymbol{L}}_{\text{ext}}$ in (22) is neglected to analyze the errors in Patterns II and III, whereas the term $\boldsymbol{\eta}$ is retained and becomes the main factor. The steady-state phase of the tracking error ${}^{\Sigma}\boldsymbol{e}$ becomes ${}^{\Sigma}\boldsymbol{K}_{\text{p}}^{-1}{}^{\Sigma}\hat{\boldsymbol{M}}^{-1}\dot{\boldsymbol{\eta}}$, implying that the steady-state error is mainly related to the modeling error and noise.

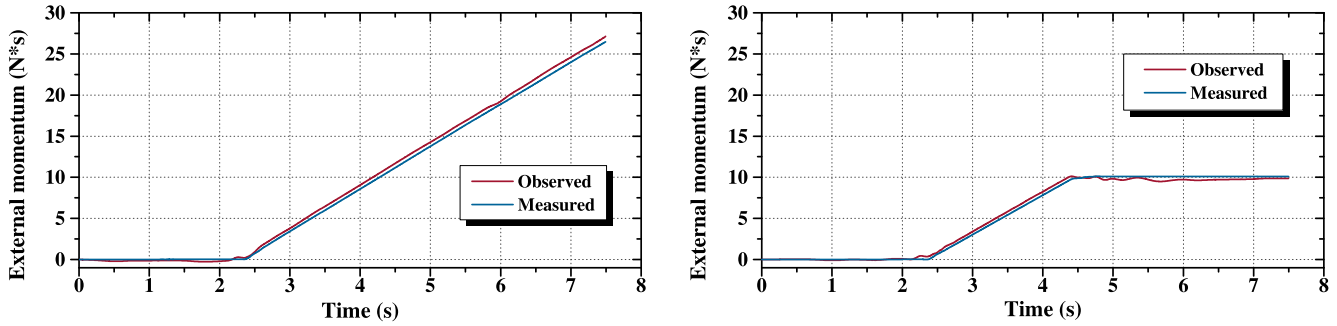

(a) Result of Pattern II. (b) Result of Pattern III.

FIGURE 7. Comparison between the observed and measured external momenta. For brevity, the external momentum along the z-axis is shown. The results of Patterns II and III are shown in (a) and (b), respectively.

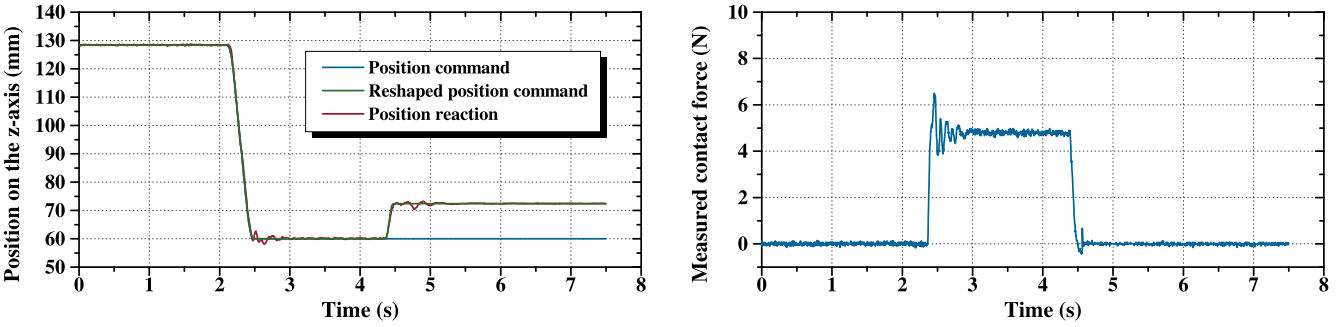

(a) Position on the z-axis. (b) Measured contact force.

FIGURE 8. Reshaped position command and contact force of Pattern III. (a) Position command, reshaped position command, and position reaction along the z-axis. (b) Contact force along the z-axis measured by the force sensor.

TABLE 3. Description of tracking errors.

Period	0 to 2.2 s	2.2 to 2.5 s	2.5 s to the end
Position errors in Pattern I	Errors on x-, y-, and z-axis approximated to 0 mm.	Errors on y- and z-axis vabriated, and the error in z-axis showed the maximum peak.	Errors on x-, y-, and z-axis attended to -1, 1, and -3 mm, respectively.
Position errors in Pattern II	Errors on x-, y-, and z-axis approximated to 0 mm.	Errors on y- and z-axis vabriated, and both errors in y- and z-axis showed the maximum peak.	Errors on x-, y-, and z-axis attended to 0.5, 1, and 0 mm, respectively.
Orientation errors in Pattern I	Errors on x-, y-, and z-axis approximated to 0 rad.	Errors on y-axis vabriated and showed the maximum peak.	Errors on x-, y-, and z-axis attended to 0.01, -0.004, and -0.005 rad, respectively.
Orientation errors in Pattern II	Errors on x-, y-, and z-axis approximated to 0 rad.	Errors on y-axis vabriated and showed the maximum peak.	Errors on x-, y-, and z-axis attended to 0.01, -0.004, and 0 rad, respectively.

In Pattern I, the contact force had the largest magnitude along the z-axis when the impactor was moved to contact and compress the dummy along the z-axis, resulting in the largest steady-state error along the z-axis. Before the impactor contacts the dummy or when the impactor compresses the dummy, a small orientation error can cause the compression direction to deviate from the z-direction. Therefore, the impactor was also subjected to the contact force along the x- and y-axis, and a steady-state error was obtained along the x- and y-axis.

Comparing Patterns I and II, the steady-state position error on the x- and z-axis decreased, and the steady-state orientation errors on z-axis was also reduced. It is concluded that feeding the estimated external momentum suppressed the steady-state error. A constant steady-state error of approximately -1 mm was obtained on the y-axis in Patterns I and II. This constant error may be attributed to the modeling error.

It should be noted that each motor actuating the CRANE-X7 manipulator has a backlash of 0.25° according to the specifications of the motors. This factor may affect the steady-state orientation and position errors. The backlash problem is considered as a type of modeling error but is not included in (23).

B. MOMENTUM OBSERVER

Fig. 7 shows the in-advanced estimation performance of the improved observer, which is opposite to the delay performance in our previous study [41]. When the estimated external momentum reached the predetermined momentum threshold, the motion reshaping was triggered to limit the estimated external momentum to a smaller value than the momentum threshold; that is, $\hat{\boldsymbol{L}}_{\text{ext}} \leq \boldsymbol{L}_{\text{index}}$, as observed in Fig. 7(b) at approximately 4.5 s. It was shown in [41] that the delayed performance made the estimated external momentum slightly exceed the measured one when the motion reshaping was triggered. However, this study shows that the in-advanced performance guarantees $\hat{\boldsymbol{L}}_{\text{ext}} \leq \boldsymbol{L}_{\text{index}}$ all the time. As a result, the safety performance is enhanced as the measured external momentum is limited much better under the estimated one. In addition, the in-advance estimation performance is due to the modification of the transfer function: adding the term $s^{\Sigma}\boldsymbol{K}_2$ is equivalent to adding the term $s^{\Sigma}\boldsymbol{K}_2(s^2 + s^{\Sigma}\boldsymbol{K}_2 + {}^{\Sigma}\boldsymbol{K}_1)^{-1}\boldsymbol{L}_{\text{ext}}$ to the estimated external momentum $\hat{\boldsymbol{L}}_{\text{ext}}$ to increase it.

C. MOTION RESHAPING

The reference momentum $\boldsymbol{L}_{\text{ref}}$ is used to power the manipulator to realize movement and resist contact forces. In a contact situation, $\boldsymbol{L}_{\text{ref}}$ can be divided into three parts: the momentum contributed by movement ${}^{\Sigma}\hat{\boldsymbol{M}}\dot{\boldsymbol{x}}_{\text{cmd}}$, momentum injury onset threshold $\boldsymbol{L}_{\text{index}}$, and momentum over the injury onset threshold $\boldsymbol{L}_{\text{adj}}$, as shown in (26). The first part ${}^{\Sigma}\hat{\boldsymbol{M}}\dot{\boldsymbol{x}}_{\text{cmd}}$ ensures that the manipulator moves along the command trajectory. Contact is limited within the momentum injury onset threshold to guarantee the safety of the human soft tissue; therefore, the second part $\boldsymbol{L}_{\text{index}}$ is permitted but the third part $\boldsymbol{L}_{\text{adj}}$ needs to be eliminated. As shown in (17), $\boldsymbol{L}_{\text{adj}}$ denoting the momentum over the injury onset threshold is transformed into a velocity signal as ${}^{\Sigma}\hat{\boldsymbol{M}}_{\text{inv}}\boldsymbol{L}_{\text{adj}}$. Specifically, part of the estimated external momentum that exceeds the momentum injury onset threshold is transformed into a trajectory motion signal to reshape the original motion command. Equation (27) shows that motion reshaping eliminates momentum over the injury onset threshold $\boldsymbol{L}_{\text{adj}}$. Therefore, the external momentum is bounded in a safe zone, $\boldsymbol{L}_{\text{ext}} \in [0, \boldsymbol{L}_{\text{index}}]$. The experimental results in Fig. 7(b) show that the motion reshaping method successfully limited the external momentum below the injury onset threshold.

D. ADVANTAGES

In our previous study [41], simulation tests were conducted to demonstrate the effectiveness of the proposed control strategy, and a delay in the estimated external momentum reduced the safety performance. As an extension of the previous study, the present work overcomes the limitation of the momentum observer by changing its structure, and validates the feasibility of the proposed control strategy on a 7-DOF manipulator in the worst case of pHRIs, that is, the clamping scenario.

The momentum controller was proposed by Ohnishi et al. [27], [28] to show the effectiveness and stability when the manipulator passes through singularity points, and the effectiveness was tested on a 2-DOF manipulator in a gravity-free and noncontact environment. However, this study first uses the momentum controller for safety and proposes a modified version. The momentum controller was modified in comparison to [28] by adding a compensator for gravity along with a part of the Coriolis and centrifugal force, represented by $\hat{\boldsymbol{g}}(\boldsymbol{\theta})$ and $-\hat{\boldsymbol{C}}^T(\boldsymbol{\theta}, \dot{\boldsymbol{\theta}})\dot{\boldsymbol{\theta}}$, respectively, in (10). Experimental results showed that the momentum controller was stable and performed well in trajectory tracking in a gravity and contact environment.

As (24) analyzed, the momentum observer is designed as a second-order low-pass filter to denoise the external momentum. Compared to our previous study [41], the momentum observer was improved by adding a derivative term to the numerator of the transfer function. Consequently, the momentum observer exhibited an in-advance estimation performance such that the measured external momentum was more limited than the estimated external momentum. This improvement enhanced the safety performance of the proposed control strategy.

The proposed control strategy provides a safety function for limiting external momentum under the momentum injury onset threshold. Such a safety function can be realized by setting a saturator inside the controller to limit the momentum reference signal. However, stability is not guaranteed because the saturated reference signal may lose its ability to adjust the tracking error. This study presents a motion reshaping method placed outside the controller loop to keep the controller stable and realize the momentum-limit function.

The momentum-limit function exhibits better performance in the under-contact period than the force-limit method. The momentum limit means that the integral of the contact force does not exceed a threshold; that is, the contact force must become zero or negative when the momentum reaches the threshold. It should be noted that in a clamping situation, a negative contact force does not exist if there is no collision in the direction opposite to clamping. Therefore, the momentum-limit function reduces the contact force to zero so that the human body part can be released from a clamping situation. This analysis is consistent with the results shown in Fig. 8(b). However, the force-limit method makes the contact force equal to or smaller than a threshold, such that the human soft tissue remains firmly constrained.

Motion reshaping was proposed based on the property of the momentum variable; that is, momentum is equal to the integral of force or the product of mass and velocity. As shown by (17), only the mass matrix is used. Owing to the property of the momentum variable, the proposed control strategy does not need to identify the mechanical properties of the human body part, can reduce the contact force to zero in a clamping situation, and can secure the safety of human body parts even in a post-contact period.

In Section II-A, we first show that the physical quantity of momentum is appropriate as a quantification criterion when considering the occurrence or nonoccurrence of a slight injury as a limit of intrinsic safety. This had an advancement compared with [21], which showed that mass and maximum velocity of the impactor were positively correlated with the injury level but no in-depth analysis regarding momentum were conducted.

E. PERFORMANCE LIMITATIONS

Since the ultimate goal of this study involves human–robot collision safety, a very low-powered manipulator was used. An industrial manipulator provides a much larger contact force compared with the CRANE-X7 manipulator. The effectiveness of the proposed control strategy needs to be tested using a high-power manipulator. Moreover, the proposed control strategy provides a safety function for a high-DOF manipulator, but the performance of the controller was not the main goal of the study. The precision of the controller performance can be enhanced by reducing the modeling errors and introducing advanced control algorithms like adaptive control or robust control.

VI. CONCLUSION

This study proposed a control strategy for securing the safety of human body parts in a clamping situation. It is shown that the momentum variable is an appropriate criterion for estimating the occurrence of a slight injury. The control strategy was developed to provide a momentum-limit function to help avoid the risk of the momentum exceeding an injury onset threshold when a human body part is clamped. Specifically, the control strategy comprises three parts: the controller loop, momentum observer, and motion reshaping. The controller loop guarantees operation-space motion trajectory tracking. The momentum observer was designed as a second-order filter to estimate the external momentum that denotes the integral of the contact force. The estimated external momentum was fed into the controller loop to eliminate the steady-state tracking error. Based on the property of the momentum variable, the part in the estimated external momentum that exceeds the injury onset threshold is transformed into a motion trajectory to reshape the command motion and limit the external momentum under the momentum injury onset threshold. Thus, the momentum observer and motion reshaping provide a momentum-limit function, which realizes the securement of safety.

A clamping experiment validated the proposed control strategy. The end effector of the CRANE-X7 manipulator was redesigned as a hexagonal prism impactor, and a dummy with high biofidelity was used as a human hand substitute to mimic the bolt-fixing task. The experimental results showed that the tracking error was suppressed within 2.5 mm, and the external momentum was successfully limited within a predetermined momentum threshold of 10 N·s. Moreover, a 5 N contact force in the clamping scenario became 0 N when the external momentum was limited. The proposed control strategy can help avoid the risk of the momentum exceeding the injury onset threshold when the human body part is clamped and can release the human body part in a clamping scenario.

Owing to ethical considerations, a dummy with high biofidelity was used to substitute the soft tissue on the human hand in the clamping experiment. The integral of the contact force, or the external momentum, as defined in this study, can be limited under a threshold using the proposed control strategy. Furthermore, it was difficult to limit the contact force itself. Future work will focus on combining the momentum-limit function and force-limit method and examining the effectiveness of the control strategy on human soft tissue.

ACKNOWLEDGMENT

The authors sincerely thank Prof. Kaoru Isogai for his advice on injury estimation and Dr. Tatsuo Fujikawa for providing the experimental data for exploring the momentum criterion for the injury onset level. In addition, the help extended by Prof. Yasuhiro Akiyama and Dr. Pengcheng Li for controller tuning is acknowledged. The authors would also like to thank Toyota Motor Corporation for providing opportunities to visit the factories and its employees for fruitful discussions.

REFERENCES

[1] Z. Liu, X. Wang, Y. Cai, W. Xu, Q. Liu, Z. Zhou, and D. T. Pham, "Dynamic risk assessment and active response strategy for industrial human–robot collaboration," *Comput. Ind. Eng.*, vol. 141, Mar. 2020, Art. no. 106302.

[2] M. Raessa, J. C. Y. Chen, W. Wan, and K. Harada, "Human-in-the-loop robotic manipulation planning for collaborative assembly," *IEEE Trans. Autom. Sci. Eng.*, vol. 17, no. 4, pp. 1800–1813, Oct. 2020.

[3] M. Webster, D. Western, D. Araiza-Illan, C. Dixon, K. Eder, M. Fisher, and A. G. Pipe, "A corroborative approach to verification and validation of human–robot teams," *Int. J. Robot. Res.*, vol. 39, no. 1, pp. 73–99, Jan. 2020.

[4] B. Siciliano, O. Khatib, and T. Kröger, *Springer Handbook of Robotics*, vol. 200. Berlin, Germany: Springer, 2008.

[5] M. Zhdanova, V. Voronin, E. Semenishchev, Y. Ilyukhin, and A. Zelensky, "Human activity recognition for efficient human–robot collaboration," *Proc. SPIE*, vol. 11543, pp. 94–104, Oct. 2020.

[6] V. V. Unhelkar, S. Li, and J. A. Shah, "Semi-supervised learning of decision-making models for human–robot collaboration," in *Proc. Conf. Robot Learn.*, 2020, pp. 192–203.

[7] M. El-Shamouty, X. Wu, S. Yang, M. Albus, and M. F. Huber, "Towards safe human–robot collaboration using deep reinforcement learning," in *Proc. IEEE Int. Conf. Robot. Autom. (ICRA)*, May 2020, pp. 4899–4905.

[8] N. Nikolakis, V. Maratos, and S. Makris, "A cyber physical system (CPS) approach for safe human–robot collaboration in a shared workplace," *Robot. Comput.-Integr. Manuf.*, vol. 56, pp. 233–243, Apr. 2019.

[9] E. Kim, Y. Yamada, S. Okamoto, M. Sennin, and H. Kito, "Considerations of potential runaway motion and physical interaction for speed and separation monitoring," *Robot. Comput.-Integr. Manuf.*, vol. 67, Feb. 2021, Art. no. 102034.

[10] J. Saenz, R. Behrens, E. Schulenburg, H. Petersen, O. Gibaru, P. Neto, and N. Elkmann, "Methods for considering safety in design of robotics applications featuring human–robot collaboration," *Int. J. Adv. Manuf. Technol.*, vol. 107, nos. 5–6, pp. 2313–2331, Mar. 2020.

[11] M. Safeea and P. Neto, "Minimum distance calculation using laser scanner and IMUs for safe human–robot interaction," *Robot. Comput.-Integr. Manuf.*, vol. 58, pp. 33–42, Aug. 2019.

[12] G. M. Vyas, A. André, and R. Sala, "Toward lightweight smart automotive hood structures for head impact mitigation: Integration of active stiffness control composites," *J. Intell. Mater. Syst. Struct.*, vol. 31, no. 1, pp. 71–83, Jan. 2020.

[13] A. Ajoudani, N. G. Tsagarakis, and A. Bicchi, "On the role of robot configuration in Cartesian stiffness control," in *Proc. IEEE Int. Conf. Robot. Autom. (ICRA)*, May 2015, pp. 1010–1016.
[14] S. Morinaga and K. Kosuge, "Collision detection system for manipulator based on adaptive impedance control law," in *Proc. IEEE Int. Conf. Robot. Autom.*, Sep. 2003, pp. 1080–1085.
[15] N. Hogan, "Impedance control: An approach to manipulation," in *Proc. Amer. Control Conf.*, 1984, pp. 304–313.
[16] C.-C. Cheah and D. Wang, "Learning impedance control for robotic manipulators," *IEEE Trans. Robot. Autom.*, vol. 14, no. 3, pp. 452–465, Jun. 1998.
[17] A. Alcocer, A. Robertsson, A. Valera, and R. Johansson, "Force estimation and control in robot manipulators," *IFAC Proc. Volumes*, vol. 36, no. 17, pp. 55–60, Sep. 2003.
[18] K. Ohishi, M. Miyazaki, M. Fujita, and Y. Ogino, "H_∞/observer based force control without force sensor," in *Proc. Int. Conf. Ind. Electron., Control Instrum.*, 1991, pp. 1049–1054.
[19] Y. Yamada, Y. Hirasawa, S. Y. Huang, and Y. Umetani, "Fail-safe human/robot contact in the safety space," in *Proc. 5th IEEE Int. Workshop Robot Human Commun.*, Jun. 1996, pp. 59–64.
[20] K. Suita, Y. Yamada, N. Tsuchida, K. Imai, H. Ikeda, and N. Sugimoto, "A failure-to-safety 'Kyozon' system with simple contact detection and stop capabilities for safe human-autonomous robot coexistence," in *Proc. IEEE Int. Conf. Robot. Autom.*, vol. 3, May 1995, pp. 3089–3096.
[21] S. Haddadin, A. Albu-Schaffer, A. De Luca, and G. Hirzinger, "Collision detection and reaction: A contribution to safe physical human–robot interaction," in *Proc. IEEE/RSJ Int. Conf. Intell. Robots Syst.*, Sep. 2008, pp. 3356–3363.
[22] A. De Luca, A. Albu-Schaffer, S. Haddadin, and G. Hirzinger, "Collision detection and safe reaction with the DLR-III lightweight manipulator arm," in *Proc. IEEE/RSJ Int. Conf. Intell. Robots Syst.*, Oct. 2006, pp. 1623–1630.
[23] P. Aivaliotis, S. Aivaliotis, C. Gkournelos, K. Kokkalis, G. Michalos, and S. Makris, "Power and force limiting on industrial robots for human–robot collaboration," *Robot. Computer-Integrated Manuf.*, vol. 59, pp. 346–360, Oct. 2019.
[24] *Robots and Robotic Devices—Collaborative Robots*, Standard ISO/TS 15066, International Organization for Standardization, 2016.
[25] S. He, J. Ye, Z. Li, S. Li, G. Wu, and H. Wu, "A momentum-based collision detection algorithm for industrial robots," in *Proc. IEEE Int. Conf. Robot. Biomimetics (ROBIO)*, Dec. 2015, pp. 1253–1259.
[26] S. Haddadin, S. Haddadin, A. Khoury, T. Rokahr, S. Parusel, R. Burgkart, A. Bicchi, and A. Albu-Schäffer, "On making robots understand safety: Embedding injury knowledge into control," *Int. J. Robot. Res.*, vol. 31, no. 13, pp. 1578–1602, 2012.
[27] S. Sakaino and K. Ohnishi, "A composition of decoupling motion controller based on momentum and its application for singular configurations," in *Proc. 33rd Annu. Conf. IEEE Ind. Electron. Soc.*, Nov. 2007, pp. 2331–2336.
[28] S. Sakaino and K. Ohnishi, "An analysis of force control based on momentum," in *Proc. 10th IEEE Int. Workshop Adv. Motion Control*, Mar. 2008, pp. 354–359.
[29] A. De Luca and R. Mattone, "Actuator failure detection and isolation using generalized momenta," in *Proc. IEEE Int. Conf. Robot. Autom.*, vol. 1, Sep. 2003, pp. 634–639.
[30] C.-N. Cho, J.-H. Kim, S.-D. Lee, and J.-B. Song, "Collision detection and reaction on 7 DOF service robot arm using residual observer," *J. Mech. Sci. Technol.*, vol. 26, no. 4, pp. 1197–1203, Apr. 2012.
[31] V. Sotoudehnejad, A. Takhmar, M. R. Kermani, and I. G. Polushin, "Counteracting modeling errors for sensitive observer-based manipulator collision detection," in *Proc. IEEE/RSJ Int. Conf. Intell. Robots Syst.*, Oct. 2012, pp. 4315–4320.
[32] Y. Tian, Z. Chen, T. Jia, A. Wang, and L. Li, "Sensorless collision detection and contact force estimation for collaborative robots based on torque observer," in *Proc. IEEE Int. Conf. Robot. Biomimetics (ROBIO)*, Dec. 2016, pp. 946–951.
[33] T. Ren, Y. Dong, D. Wu, and K. Chen, "Collision detection and identification for robot manipulators based on extended state observer," *Control Eng. Pract.*, vol. 79, pp. 144–153, Oct. 2018.
[34] S.-D. Lee, M.-C. Kim, and J.-B. Song, "Sensorless collision detection for safe human–robot collaboration," in *Proc. IEEE/RSJ Int. Conf. Intell. Robots Syst. (IROS)*, Sep. 2015, pp. 2392–2397.
[35] J. Xiao, Q. Zhang, Y. Hong, G. Wang, and F. Zeng, "Collision detection algorithm for collaborative robots considering joint friction," *Int. J. Adv. Robotic Syst.*, vol. 15, no. 4, Jul. 2018, Art. no. 172988141878899.
[36] G. Garofalo, N. Mansfeld, J. Jankowski, and C. Ott, "Sliding mode momentum observers for estimation of external torques and joint acceleration," in *Proc. Int. Conf. Robot. Autom. (ICRA)*, 2019, pp. 6117–6123.
[37] S. Long, X. Dang, S. Sun, Y. Wang, and M. Gui, "A novel sliding mode momentum observer for collaborative robot collision detection," *Machines*, vol. 10, no. 9, p. 818, Sep. 2022.
[38] T. Fujikawa, R. Sugiura, R. Nishikata, and T. Nishimoto, "Critical contact pressure and transferred energy for soft tissue injury by blunt impact in human–robot interaction," in *Proc. 17th Int. Conf. Control, Autom. Syst. (ICCAS)*, Oct. 2017, pp. 867–872.
[39] B. Siciliano, L. Sciavicco, L. Villani, and G. Oriolo, *Robotics: Modelling, planning and control*. Berlin, Germany: Springer, 2009.
[40] A. De Luca and L. Ferrajoli, "A modified Newton–Euler method for dynamic computations in robot fault detection and control," in *Proc. IEEE Int. Conf. Robot. Autom.*, May 2009, pp. 3359–3364.
[41] J. Liu, Y. Yamada, Y. Akiyama, S. Okamoto, and Y. Iki, "A novel safety-oriented control strategy for manipulators based on the observation and adjustment of the external momentum," in *Proc. Int. Conf. Comput., Control Robot. (ICCCR)*, 2021, pp. 80–86.
[42] J. Liu, Y. Yamada, and Y. Akiyama, "Calculating the supplied energy for physical human–robot interaction," in *Proc. IEEE Int. Conf. Intell. Safety Robotics (ISR)*, Sep. 2021, pp. 157–160.
[43] W. Khalil and E. Dombre, *Modeling Identification and Control of Robots*. Boca Raton, FL, USA: CRC Press, 2002.
[44] Y. Iki, Y. Yamada, Y. Akiyama, S. Okamoto, and J. Liu, "Designing a dummy skin by evaluating contacts between a human hand and a robot end tip," in *Proc. IEEE/RSJ Int. Conf. Intell. Robots Syst. (IROS)*, Oct. 2020, pp. 11337–11344.
[45] J. Liu, Y. Yamada, Y. Akiyama, S. Okamoto, and Y. Iki, "Development of dummy based on impedance properties of human soft tissue using a nonlinear viscoelastic model," *IEEE Access*, vol. 11, pp. 7782–7793, 2023.
[46] R. Kelly, "A tuning procedure for stable PID control of robot manipulators," *Robotica*, vol. 13, no. 2, pp. 141–148, Mar. 1995.

JIAN LIU received the M.S. degree in mechanical and electronic engineering from Zhejiang University, Hangzhou, China, in 2018. He is currently pursuing the Ph.D. degree in mechanical systems engineering with Nagoya University, Nagoya, Japan. In 2023, he joined Nagoya University as a Researcher. His current research interests include robotics, biomechanics, and especially physical human safety in human–robot coexistence systems.

YOJI YAMADA (Member, IEEE) received the Ph.D. degree from the Tokyo Institute of Technology. Since 1983, he has been with the Toyota Technological Institute, Nagoya, Japan, as an Assistant Professor. In 2004, he joined the Safety Intelligence Research Group, National Institute of Advanced Industrial and Science Technology (AIST), as a Leader. In 2009, he joined the Department of Mechanical Science and Engineering, Graduate School of Engineering, Nagoya University, as a Professor. In 2022, he joined the Toyota College, National Institute of Technology, as a President.